Conclusions

We presented numerical simulation results for flow past fixed and freely-vibrating cylinders, using a Chimera Reynolds-averaged Navier-Stokes method. The predicted Drag vs. Reynolds number curve for fixed cylinders was found to be in good agreement with experimental measurements at sub-, trans-, and super-critical flow conditions.

For freely-vibrating light structures with low damping exposed to high Reynolds number flow conditions, cross-stream amplitudes of 1.5 cylinder diameters are observed. At a Reynolds number of 1×10^5 in-line amplitudes of 0.35 cylinder diameters are observed, with a significant increase in the average drag coefficient. At a Reynolds number of 1×10^6 the in-line oscillations are significantly smaller with amplitudes of 0.05 cylinder diameters.

Acknowledgements

Computations were performed using resources of the Texas A&M Supercomputer Facility, their support is acknowledged. The support from the Department of Interior, Minerals Management Service (MMS) and the Offshore Technology Research Center (OTRC) is gratefully acknowledged.

References

Bearman P. W. (1969). "On vortex shedding from a circular cylinder in the critical Reynolds number regime." *Journal of Fluid Mechanics,* 37(3), 577-585.

Chen H. C. and Patel V. C. (1988). "Near-wall turbulence models for complex flows including separation." *AIAA Journal,* 26(4), 641-648.

Henderson R. D. (1995). "Details on the drag curve near the onset of vortex shedding." *Physics of Fluids,* 7, 2102-2104.

Pontaza, J. P., Chen H. C., and Reddy J. N. (2004). "A local-analytic-based discretization procedure for the numerical solution of viscous incompressible flows." *International Journal for Numerical Methods in Fluids,* submitted.

Roshko A. (1961). "Experiments on the flow past a circular cylinder at very high Reynolds number." *Journal of Fluid Mechanics,* 10, 345-356.

Sani R. L. and Gresho P. M. (1994). "Resume and remarks on the open boundary condition minisymposium." *International Journal for Numerical Methods in Fluids,* 18, 983-1008.

Time-Domain Simulation of Four-Quadrant Propeller Flows by a Chimera Moving Grid Approach

H. C. Chen[1] and Sing-Kwan Lee[2]

[1]Ocean Engineering Program, Department of Civil Engineering, Texas A&M University, College Station, Texas 77843; email: hcchen@civil.tamu.edu
[2]Research and Product Development, Technology, American Bureau of Shipping, ABS Plaza, 16855 NorthChase Drive, Houston, 77060; email: SLee@eagle.org

Abstract

A Reynolds-Averaged Navier-Stokes (RANS) method has been employed in conjunction with a chimera moving grid approach to provide accurate resolution of four-quadrant propeller flows under both the design and off-design conditions. Time-domain simulations were performed first for the DTRC 4118 propeller under ahead, bollard-pull, crash-ahead, crash-astern, and backing conditions and compared with the available experimental data. Preliminary numerical results were also presented for the DTRC 4383 propeller to illustrate the applicability of the chimera RANS method for highly skewed propellers.

Introduction

The potential flow methods based on the assumptions of inviscid fluid and irrotational motion are widely used in propeller flow analysis (Kerwin and Lee, 1978; Greeley and Kerwin, 1982; Kosal et al., 1998). However, some off-design propeller flow phenomena are dominated by viscous effects and cannot be accurately predicted by the potential flow methods. Off-design conditions include all four quadrants as defined by the ship velocity V_s and the propeller angular velocity ω. The four modes of propeller operation are defined as ahead or forward ($+V_s$, $+\omega$), backing or astern ($-V_s$, $-\omega$), crash-ahead or reverse backing ($-V_s$, $+\omega$) and crashback or crash-astern ($-V_s$, $+\omega$). During crash-astern and crash-ahead operations, the reversal of propeller rotation creates a relatively large angle of attack, causing the flow to separate at the leading edge of the blade. The water tunnel measurements performed by Jiang et al. (1997) demonstrated that the flow is unsteady even when the propeller is operated in the steady crash-astern condition. Furthermore, the propeller inflow is strongly affected by the unsteady stern boundary layer flow generated by the braking or turning maneuvers of the ship during crash-astern operations. It is therefore desirable to use advanced viscous flow methods in order to provide more accurate resolution of the propeller flow in off-design conditions.

Jiang et al. (1991) extended the inviscid-flow propeller design methods for the simulation of backing and crash-astern conditions. They adopted a simplified approach in propeller flow analysis program PSF by assuming that the blade pressure distribution is some factor of the pressure distribution when there is no separation. Although this simplified method can correlate the calculated thrust and torque with measurements in certain range of advance coefficient through a camber correction factor, the real blade pressure distribution cannot be predicted. A recent study by Chen and Stern (1999) suggested that more sophisticated viscous flow methods are needed in order to improve the prediction of propeller performance under crash-ahead and crash-astern conditions.

Besides the crash-astern propeller flow problem, the viscous flow model is also needed to quantify the damping effect of a propeller. Viscous damping is an important factor for torsional vibration damping of ship's propulsion system. In fact, in addition to the excited forces/moments of the propeller blades and the added mass of the entrained water, damping is an important input to propulsion shaft vibration analyses. Although for initial design purpose regression formula (Parsons and Vorus, 1981) are available for added mass and damping estimate, the applicability of them is restricted to the 4-, 5-, 6-, and 7- Wageningen B Screw series geometry with the expanded area ratios in the range of 0.5 to 1.0 and pitch ratios in the range of 0.6 to 1.2. Also, viscous damping is not included in the damping coefficients of Parsons and Vorus's regression formula. In order to properly account for viscous effects, it is necessary to employ accurate and robust numerical methods which can provide detailed resolution of the propeller boundary layer, turbulent wake, leading edge separation, and unsteady ring vortices induced by propeller operations under off-design conditions.

Numerical Method

The present chimera RANS method solves the Reynolds-Averaged Navier-Stokes equations for incompressible flow in general curvilinear coordinates (ξ^i, t):

$$U^i_{,i} = 0 \tag{1}$$

$$\frac{\partial U^i}{\partial t} + U^j U^i_{,j} + \overline{u^i u^j}_{,j} = f^i - g^{ij} p_{,j} - \frac{1}{\text{Re}} g^{jk} U^i_{,jk} \tag{2}$$

where U^i and u^i represent the mean and fluctuating velocity components, and g^{ij} is the conjugate metric tensor. t is time p is pressure, f^i are the body forces, and $\text{Re} = U_o L/\nu$ is the Reynolds number based on a characteristic length L, a reference velocity U_o, and the kinematic viscosity ν. Equations (1) and (2) represent the continuity and mean momentum equations, respectively. The equations are written in tensor notation with the subscripts, $,j$ and $,jk$, represent the covariant derivatives. In the present study, the two-layer turbulence model of Chen and Patel (1988) is employed to provide closure for the

Reynolds stress tensor $\overline{u^i u^j}$. More details of the chimera RANS method are given in Chen and Liu (1999), Chen et al. (2000, 2002) and Chen and Lee (2003).

In the present study, the RANS method has been employed in conjunction with a chimera moving grid approach for time-domain simulation of two selected propeller configurations under open water conditions. Calculations were performed for both the design and off-design conditions including ahead, backing, bollard-pull, crash-ahead, and crash-astern conditions. Details of the numerical results are presented in the next section.

Results and Discussion

Calculations were performed first for the DTRC 4118 propeller as shown in Figure 1. In the chimera domain decomposition approach, it is convenient to construct an overset grid system with the propeller blades and shaft grids embedded in background cylindrical grid blocks. In the present study, each propeller blade is covered by a small $82 \times 23 \times 14$ grid around the propeller root and shaft junction and a larger $82 \times 31 \times 29$ grid outside the shaft boundary layer. The propeller shaft is covered by a $71 \times 17 \times 181$ grid block. The propeller blade and shaft grid blocks are embedded in two overlapping cylindrical grids with $62 \times 26 \times 181$ and $51 \times 35 \times 181$ grid points for the upstream and downstream sections of the solution domain. For the open water propeller condition considered here, it is necessary to simulate only one propeller blade with periodic boundary conditions specified in the circumferential direction. The total number of grid points used is about 360,000 for a 122° section of the solution domain (i.e., 1/3 of the domain plus one grid layer of overlap).

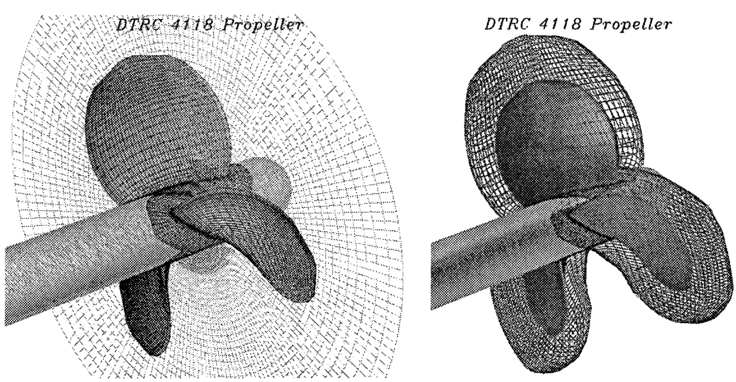

Figure 1. Multi-block chimera grids for DTRC 4118 propeller

For the open water propeller flow computations, it is possible to solve the propeller flow on a non-rotating coordinate system with fixed grids by including the centrifugal and Coriolis forces in the RANS equations. Alternatively, one may solve the unsteady RANS equations for the rotating propeller directly on an earth-fixed coordinate system. In the present study, the latter approach is adopted so that the method can be easily generalized for complete ship and propeller flow simulations with the propeller operating in a non-uniform ship wake. The use of rotating grid also greatly simplify the far field boundary condition where uniform flow can be specified without considering the swirling velocity components.

DTRC 4118 propeller: ahead condition

Figure 2 shows the predicted pressure distributions on the propeller blade surface under the ahead condition with an advance coefficient $J_A = 0.833$. It is clearly seen that the pressure is low on the suction side of the propeller and considerably higher on the pressure side of the blade. The pressure differences between the pressure and suction sides of the blade produced a net thrust force which pushes the propeller forward. The predicted thrust coefficient $K_T = 0.155$ is in good agreement with the corresponding measurement of $K_T = 0.15$.

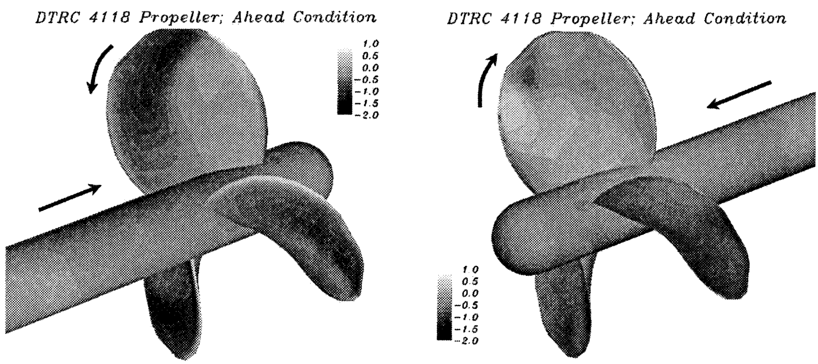

Figure 2. Pressure contours on the shaft and blades of DTRC 4118 propeller; $J_A = 0.833$

Figure 3 shows the particle traces around the DTRC 4118 propeller at $J_A = 0.833$. It is noted that the pitch of particle traces (streamlines) originated from the upstream of the propeller is much longer than those released from the blade tip or the propeller wake. This clearly indicates that the axial flow velocity is higher behind the mid-section of the propeller blade due to local flow acceleration by the propeller thrust force. In the near wake region, there is an obvious contraction of streamlines due to radial pressure gradients induced by the swirling flow behind the propeller. Immediately downstream of the propeller hub, there is a small flow separation and the fluid particles in this region were pushed back toward the propeller before being swept downstream.

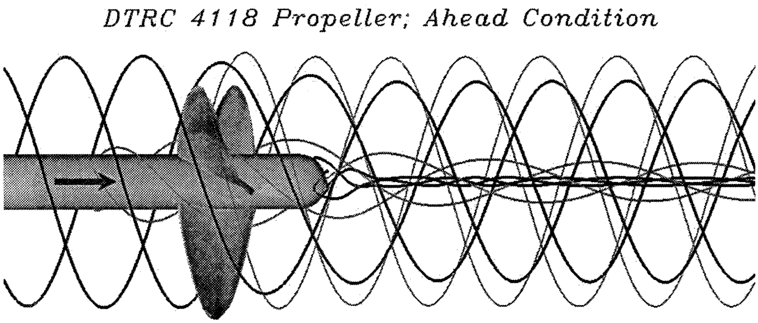

DTRC 4118 propeller: bollard-pull condition

After successful simulation of DTRC 4118 propeller under the ahead condition, calculations were also performed for various off-design propeller operations including bollard-pull, backing, crash-astern, and crash-ahead conditions. Figure 4 shows the predicted surface pressure distribution for the bollard-pull condition for the same DTRC 4118 propeller operating at zero forward speed (i.e., $J_A = 0$). It is seen that the bollard pull condition produced a much larger pressure gradient between the pressure and suction sides of the blade than that observed under the ahead condition. The predicted thrust coefficient for the bollard-pull condition is about 0.54, which is also in good agreement with the measured value of 0.52. The slightly higher predictions for both the bollard-pull and ahead conditions may be due, at least in part, to the differences in the propeller shaft geometry which is not available in the literature.

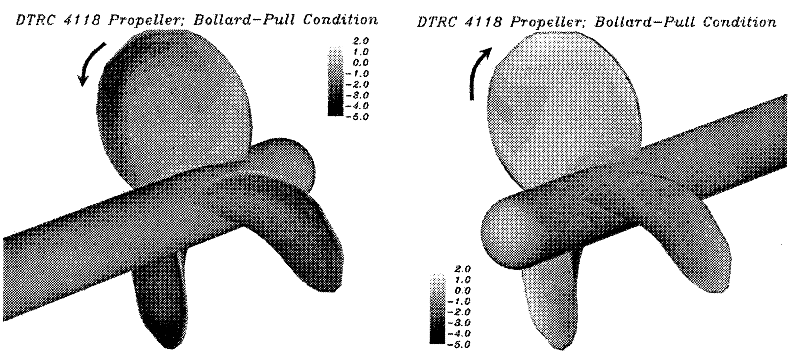

Figure 4. Pressure contours around DTRC 4118 propeller; bollard-pull condition

It is worthwhile to compare the velocity vector plots around the propeller blade for the ahead and bollard-pull conditions as shown in Figure 5. For the ahead condition at $J_A = 0.833$, the inflow is aligned closely with the designed blade angle at the propeller leading edge. Under the bollard-pull condition, however, the inflow approaches the propeller leading edge with a large angle of attack. This produced a larger thrust force, but also required a larger torque for propeller operation.

Figure 6 shows the particle traces around the propeller blades under the bollard-pull condition. It is seen that the pitch is very short for streamlines far upstream or far downstream of the propeller since the axial velocity in the far field is zero. Furthermore, the streamlines close to the propeller hub have much longer pitches than those observed outside the propeller disk due to strong flow accelerations in the mid-span region of the propeller. It is also interesting to note that some of the fluid particles are trapped in the near field due to strong swirling flow and relatively weak axial velocity under bollard-pull conditions.

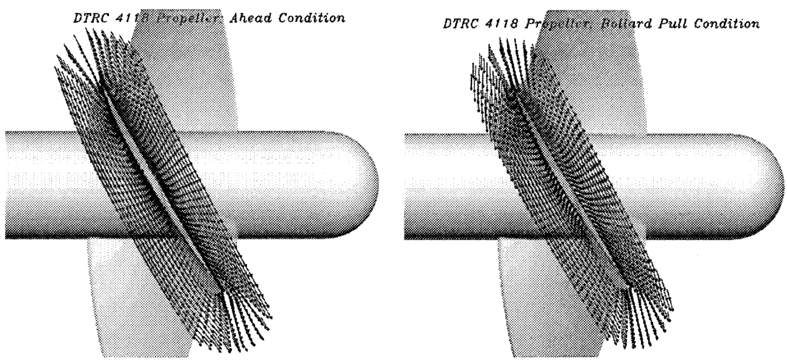

Figure 5. Velocity vectors for the ahead ($J_A = 0.833$) and bollard-pull ($J_A = 0$) conditions

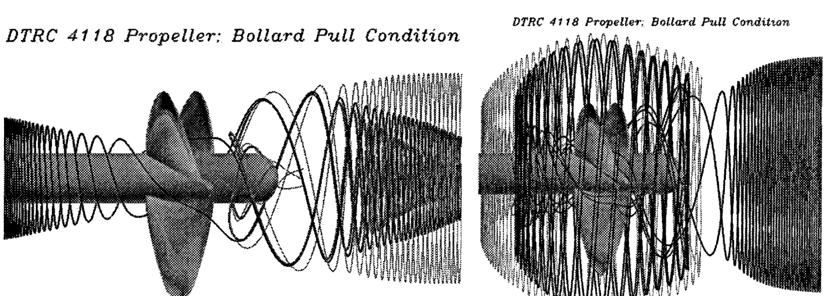

Figure 6. Particle traces around DTRC 4118 propeller under bollard pull condition

DTRC 4118 propeller: crash-ahead condition

Under the crash-ahead operations, the ship (and the propeller) is moving backward while the propeller blades are still rotating in the same direction as the ahead or bollard-pull operations. Consequently, the inflow impinges on the propeller trailing edge with a large angle of attack as shown in Figure 7 for a typical crash-ahead operation at an advance coefficient of $J_A = 0.4$. This produced large separation regions on the suction side of the propeller blades and the ring vortex generated by the crash-ahead operation is clearly visible near the blade tips. For completeness, the corresponding particle traces are also shown in Figure 8 to provide a more detailed understanding of the complex recirculating flow patterns induced by the crash-ahead operation. It is noted that some of the fluid particles originated from the upstream and the blade tip regions are trapped inside the ring vortex on the suction side of the propeller blades.

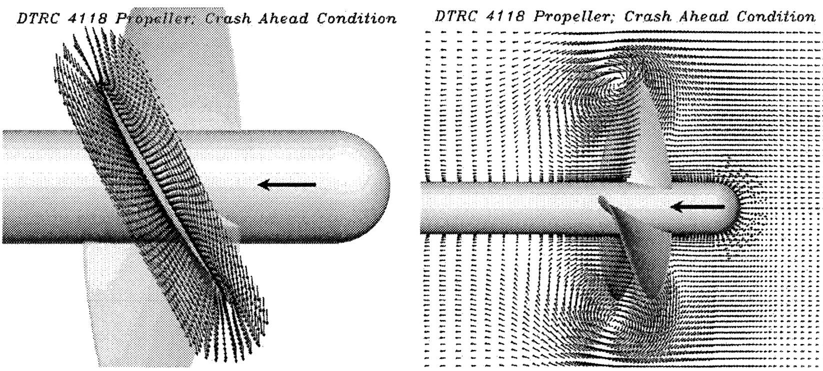

Figure 7. Velocity vector plots around DTRC 4118 propeller; crash-ahead condition

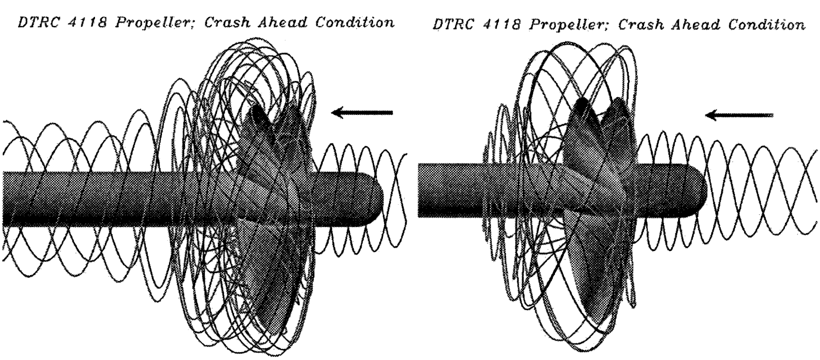

Figure 8. Particle traces around DTRC 4118 propeller; crash-ahead condition

Figure 9 shows the predicted pressure contours on the propeller shaft and blade surfaces. In general, the pressure is very low on the blade suction side and the lowest pressure was observed near the leading edge of the blade tip region. The predicted thrust coefficient is significantly higher than those obtained earlier for the ahead and bollard-pull conditions. The thrust force generated by the crash-ahead operation will slow down the ship and gradually reverse the ship direction from backward to forward motion.

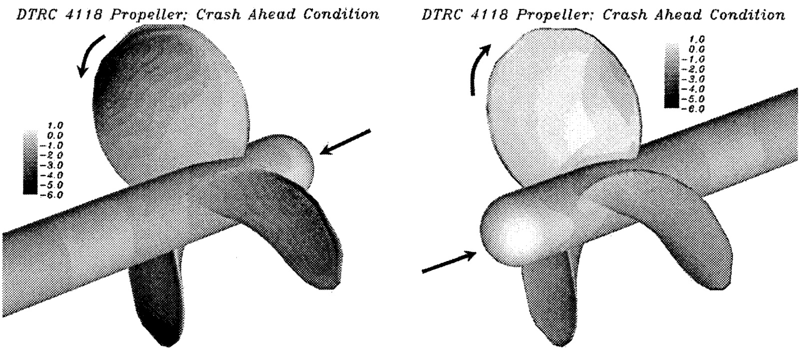

Figure 9. Pressure contours around DTRC 4118 propeller; crash-ahead condition

DTRC 4118 propeller: crash-astern condition

For the crash-astern case, the ship is moving forward but the propeller is operating in the reverse direction. This results in a large angle of attack similar to those encountered in the crash-ahead operations. Moreover, the propeller leading and trailing edges are also switched due to the reversal of propeller rotating direction. Figure 10 shows the velocity vectors around the propeller blades at an advance coefficient of J_A = 0.4. The corresponding particle traces are also shown in Figure 11 to provide a better understanding of the detailed three-dimensional flow induced by crash-astern operation. It is seen from Figure 11 that the boundary layer flow in the propeller cap region was pushed backward into the blade passages since the original propeller trailing edge becomes the leading edge now. It is further noted that the inflow impinges on the suction side of the propeller blade and separates along the blade trailing edge (i.e., leading edge in normal operation). In the mid-span region of the blade passage, a large separation region can be clearly seen on the blade pressure side. Since the flow enters the propeller passage from both the leading and trailing edges, the passage flow was pushed in the radial direction towards the blade tip and a large ring vortex was formed on the pressure side of the blade tip region. This ring vortex is similar to that observed earlier for the crash-ahead condition except that both the flow direction and vortex location are completely reversed. The similarity in the flow pattern between the crash-ahead and crash-astern conditions can also be observed from the corresponding particle traces shown in Figures 8 and 11, respectively. Under the crash-astern condition, the particles originated from the propeller hub region were pushed backward into the blade passage and then moved outward to the blade tip region before being swept downstream. Also, some of the fluid particles released from the upstream were trapped in the ring vortex similar to those observed earlier for the crash-ahead condition.

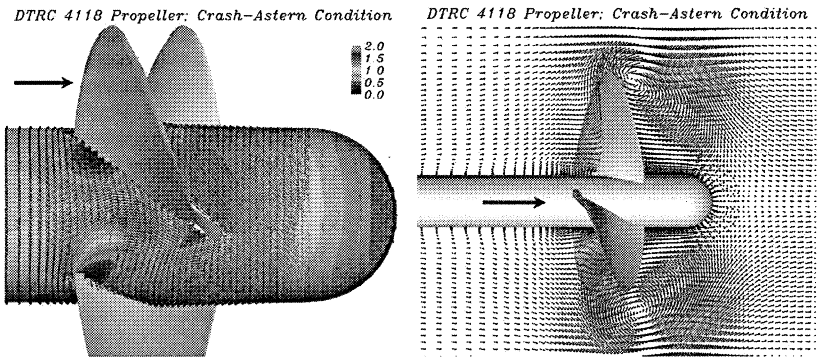

Figure 10. Velocity magnitude contours and velocity vectors around DTRC 4118 propeller; crash-astern condition

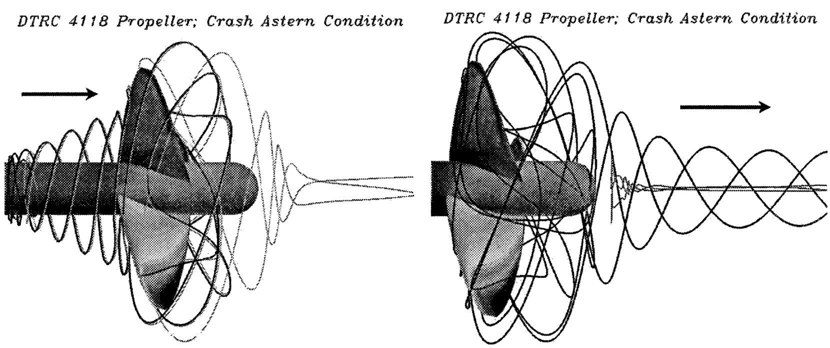

Figure 11. Particle traces around DTRC 4118 propeller; crash-astern condition

For completeness, the pressure contours on the propeller shaft and blade surfaces are also shown in Figure 12 for the crash-astern condition. It is seen that the low pressure region is shifted from the suction side to pressure side of the propeller blades in comparison with the normal ship operation under the ahead condition. This produced a negative thrust force (i.e., drag force) and a decrease of the ship forward speed during the crash-astern operations. It is also interesting to note that the pressure distributions on the